Ceramics International 44 (2018) 15851–15858

Contents lists available at ScienceDirect

Ceramics International

journal homepage: www.elsevier.com/locate/ceramint

Residual stress and microstructure effects on mechanical, tribological and electrical properties of TiN coatings on 304 stainless steel

Yeting Xi[a], Yanyun Bai[a], Kewei Gao[a], Xiaolu Pang[a,*], Huisheng Yang[a], Luchun Yan[a], Alex A. Volinsky[b]

[a] *School of Materials Science and Engineering, University of Science and Technology Beijing, Beijing 100083, PR China*
[b] *Department of Mechanical Engineering, University of South Florida, Tampa, FL 33620, USA*

ARTICLE INFO

Keywords:
Residual stress
Mechanical properties
Tribology
Electrical resistivity
Ceramic coatings
Mechanism

ABSTRACT

Mechanical, tribological and electrical properties of TiN coatings on 304 stainless steel were investigated and the effects of microstructure and residual stress on these properties were studied. Microstructure, surface roughness, hardness and preferred orientation of the coatings were investigated by AFM, SEM, nanoindentation and XRD. Residual stress of the coatings was designed and controlled in a relatively narrow range successfully using negative bias voltage based on the film thickness effect on residual stress. Residual stress was investigated by grazing-incidence X-ray diffraction using the optimized $\cos^2\alpha \sin^2\psi$ method. Friction behavior and wear characteristics were evaluated using a tribometer. The results indicate a great influence of microstructure and residual stress on the properties and service behavior of TiN coatings. Based on the experimental findings, an intermediate residual stress and proper microstructure are of vital importance to achieve better performance of coatings during service.

1. Introduction

With the development of modern industry and manufacturing technology, applications of brittle ceramic coatings are quite extensive. These protective coatings are used as mechanical components, diffusion barriers in microelectronics and decorative applications on various products [1,2]. They are widely used mainly due to their high hardness, low friction, high wear [3] and oxidation [4,5] resistance, as well as adequate anti-corrosive properties [6]. In recent years, they have also been introduced as metal gate and capacitor electrode materials because of low resistivity, relatively high process compatibility and good thermal stability [7,8]. However, hard ceramic coatings operate in harsh service environments. Failure problems prevent coatings from device integration. Most common failures are cracking, delamination and spalling [9–12]. Coating failures typically happen at high temperature, humidity, speed friction, applied stress, or a combination thereof. It is commonly accepted that the primary cause of these failures is the coatings' microstructure. As a consequence, many studies have paid attention to the effects of microstructure on the properties of coating material [13,14]. Meanwhile, some studies are focusing on the residual stress affecting coating properties.

However, few studies have analyzed the properties of coating materials from the combined view point of microstructure and residual stress. On the one hand, residual stress of magnetron sputtered coatings is always related to the microstructure due to the physical vapor deposition (PVD) process [15]. As mentioned above, the microstructure of the material determines the performance and it is an inherent property of the material. On the other hand, residual stress also has a great influence on the performance of PVD coatings [16–19].

The emphasis of this work is on mechanical, tribological, and electrical properties of the TiN coatings with different residual stress and the correlated mechanisms revealed from the aforementioned combined point of view.

2. Materials and experimental techniques

2.1. Coating deposition

TiN coatings were deposited by reactive RF-pulsed magnetron sputtering on polished SUS 304 stainless steel (304 SS) substrates. The schematic diagram of the magnetron sputtering system is shown in Fig. 1.

The substrates were cleaned in acetone for 5 min in an ultrasonic cleaner before deposition. Ar^+ ion bombardment at 100 W for 15 min was used to remove surface contamination and activate the sample's surface. The purity of the Ti target was 99.99% and the base pressure

---

* Corresponding author.
E-mail address: pangxl@mater.ustb.edu.cn (X. Pang).

https://doi.org/10.1016/j.ceramint.2018.05.266
Received 18 May 2018; Received in revised form 28 May 2018; Accepted 31 May 2018

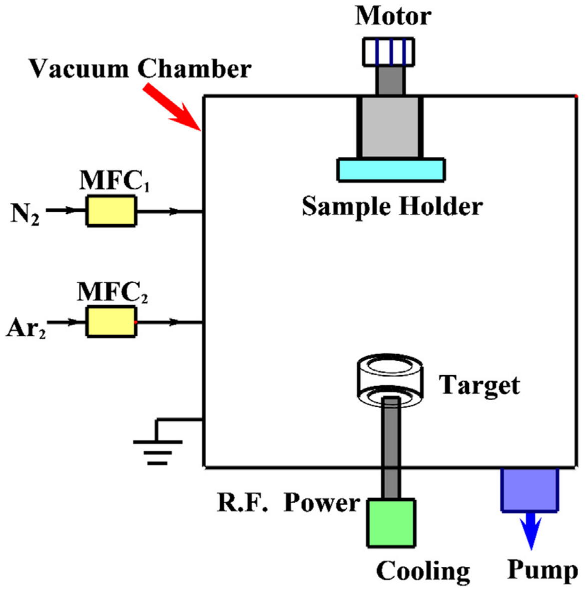

Fig. 1. Schematic diagram of the magnetron sputtering system.

was greater than 4.2 × 10^{-3} Pa. A sputtering power of 300 W for the Ti target was used. The substrate temperature during deposition was kept at 300 °C, while the working pressure was kept at 3.2 × 10^{-1} Pa. The coatings underwent a natural cooling process to room temperature in a vacuum chamber after deposition. The thickness of every coating was acquired by a 3D white light interference optical microscope (Contour GT-K, Bruker). The coating thickness was about 1.8 µm. The measurement is presented in Fig. 2.

To investigate the effect of residual stress on tribological properties, coatings with the same thickness but different residual stress were prepared by applying various negative biases to the substrates. Since the process parameters can influence the residual stress of the coatings, a bias of 0 V, − 30 V, − 60 V, − 90 V, − 120 V and − 150 V (referred as S1, S2, S3, S4, S5, S6, respectively) was applied during deposition in this study.

2.2. Coating characterization

2.2.1. Crystal structure and morphology

Crystallographic structure of the coatings was identified by X-ray diffractometry (SmartLab, Rigaku, Japan) with 40 kV and 150 mA. The wavelength of Cu $K_{\alpha1}$ radiation was 1.5406 Å. A field emission scanning electron microscope (FESEM, SUPRA 55, Zeiss) was used to observe the surface morphology of the coatings and wear tracks after tribological test.

2.2.2. Mechanical properties

The residual stress of the coatings was determined by grazing incidence X-ray diffraction (GIXRD). The measurement is based on the $\cos^2\alpha\sin^2\psi$ method, which has the same principle as the traditional $\sin^2\psi$ method. The biaxial residual stress of the coatings was determined from the lattice spacing at several inclination angles and the biaxial strain in $\cos^2\alpha\sin^2\psi$ method described in reference [20]. To ensure accuracy, asymmetric diffraction geometry and parallel beam optics were used [21]. Moreover, the advantages of the grazing incidence diffraction geometry are limiting the beam penetration depth, increasing the diffraction volume of the coatings and avoiding diffraction reflections from the substrate.

Nanoindentation with a Berkovich diamond tip (Hysitron TI 900, USA) was used to evaluate the Young's modulus and hardness of the TiN coatings. The indenter head was loaded at a constant rate of 200 µN/s,

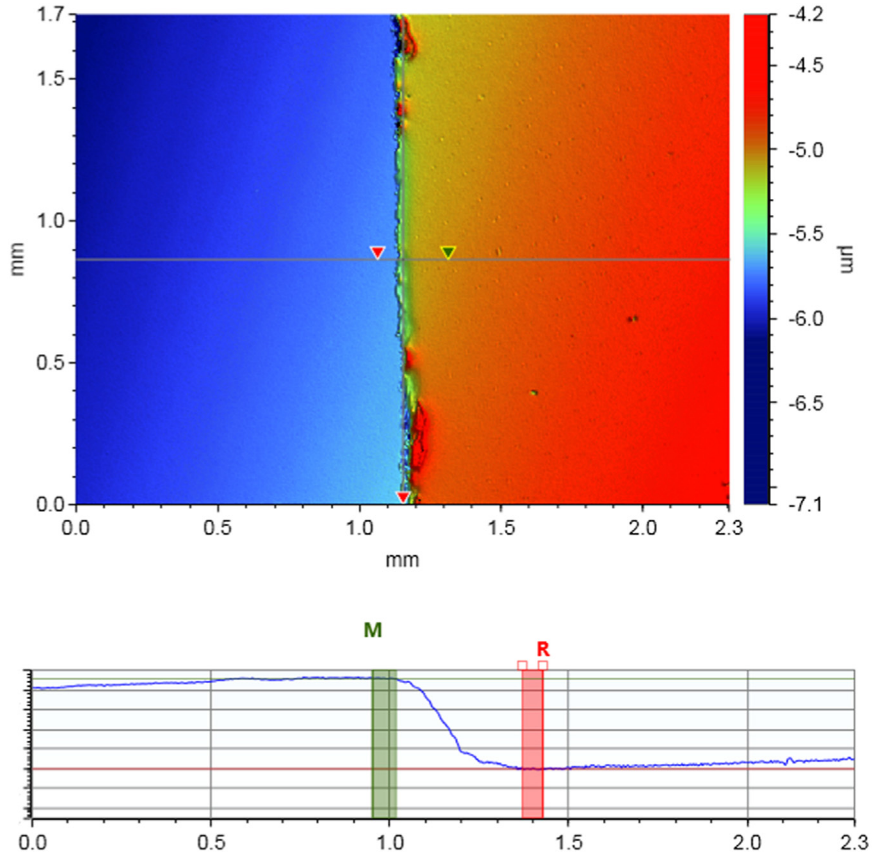

Fig. 2. Image of the coating step area and thickness profile of coating using white light interference.

reaching the maximum load of 5 mN. For every sample, five measurements were made and the average value was calculated and reported to ensure results repeatability. The indentation depth was within 10% of the coating thickness to avoid the substrate effects [22].

2.2.3. *Surface roughness and electrical resistivity*

The electrical resistivity of the coatings was measured with the four-point probe (ST2722-SZ, China). The surface roughness of the coatings was determined by an atomic force microscope (AFM, Dimension Icon, Bruker).

2.2.4. *Tribology and wear resistance*

A tribometer (UMT2, CETR, Bruker) was used to determine the coefficient of friction (COF) of the coatings at room temperature. Wear tests were carried out using Si_3N_4 balls. The applied load was 5 N. The morphology of wear tracks and the corresponding wear volume were determined by a 3D laser microscope (LEXT OLS4000, Olympus).

3. Results and discussion

3.1. *Crystal structure*

The crystal structure and grain size of the TiN coatings were determined by grazing incidence X-ray diffraction. TiN coatings have face-centered cubic (FCC) structure referenced to the standard sample (JCPDS 38-1420). The three main diffraction peaks of TiN coatings are shown in Fig. 3(a). There are peaks at 2*Theta* = 37.1°, 42.9° and 62.4°, which correspond to (111), (200), and (220) planes of TiN coatings, respectively. As seen in Fig. 3(a), the preferred orientation is (200) when the bias voltage is relatively low. When the bias voltage increased, the preferred orientation switched from (200) to (111) and (220), mainly favoring (111). Moreover, the relative texture coefficient (RTC) was used to quantify the percentage of crystal planes with a certain orientation. The calculation was based on the following equation [23,24]:

$$RTC_{(hkl)} = \frac{I_{m(hkl)}/I_{0(hkl)}}{\frac{1}{n}\sum_1^n I_{m(hkl)}/I_{0(hkl)}} \tag{1}$$

Here, $I_{m(hkl)}$ is the measured relative intensity of the (*hkl*) plane diffraction reflection, $I_{0(hkl)}$ is the relative intensity from the same plane in the standard reference sample (JCPDS 38–1420), and *n* is the total number of the main reflection peaks from the coatings. It is derived from the XRD spectra of the TiN coatings according to Eq. (1) and the results are listed in Table 1.

Fig. 3(b) clearly shows that the preferred orientation of the coatings evolved from (111) to (200) with respect to the bias voltage in a nearly linear way. Without bias voltage, (111) was the predominant orientation with an RTC of 40.4%. (220) had an RTC of 32.1%, higher than that of (200), whose RTC was 27.5%. When the bias voltage increased, the RTC of (200) increased in a nearly linear way, while the other two orientations decreased. When the bias voltage was − 30 V, the RTC of (200) was 40.5%, making it the preferred orientation. Moreover, when bias voltage absolute value was higher than − 120 V, the RTC of (200) was beyond 60%, reaching 66.7% at − 150 V. The main reason underlying such a preferred orientation transition is closely related to the total system energy. It is believed that the system tends to minimize the overall surface energy when new crystal islands are formed [25]. In our previous study, the orientation of the TiN (200) plane was proven to have the lowest surface energy [26]. The energy of the ion bombardment increases with the bias voltage during deposition. Therefore, TiN (200) with the lowest surface energy naturally becomes the dominant orientation after the energy gets larger. Consequently, the preferred orientation turns from TiN (111) to (200) to reduce both the surface energy and the total system energy.

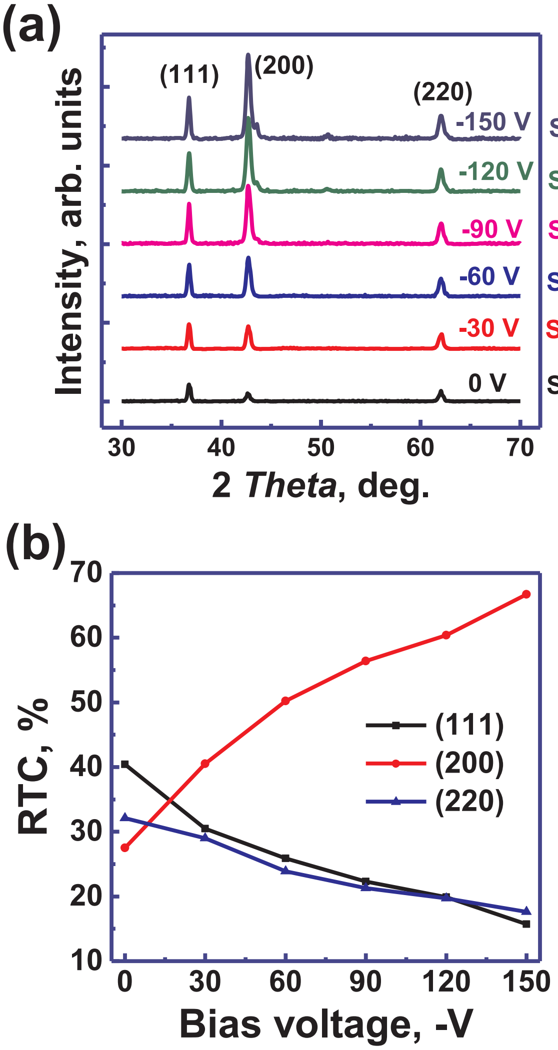

Fig. 3. (a) GIXRD spectra for TiN coatings deposited under different bias voltage; (b) RTC evolution with bias voltage.

Table 1
The relative texture coefficient evolution with bias voltage of the three main planes of the TiN coatings.

Bias voltage -V	$RTC_{(111)}$ %	$RTC_{(200)}$ %	$RTC_{(220)}$ %
0	40.4	27.5	32.1
30	30.5	40.5	29.0
60	25.9	50.2	23.9
90	22.3	56.4	21.3
120	19.9	60.4	19.7
150	15.7	66.7	17.6

3.2. *Residual stress*

The residual stress in the TiN coatings was measured by GIXRD. TiN (220) plane was chosen for the stress measurements in the 61–64° 2*Theta* range. The reason for the choice of TiN (220) should be pointed out. In the conventional XRD $\sin^2\psi$ method, high 2*Theta* diffraction angles are more suitable to be selected for the coating stress measurement because of their higher strain sensitivity. However, for highly textured PVD coatings, the diffraction peaks corresponding to a relatively large 2*Theta* angle range often have irregular shape and relatively low peak intensity. Considering the size effect and relatively low diffraction intensity of the coating materials, these shortcomings will lead

Table 2
Mechanical, tribological and electrical properties of the TiN coatings deposited under different bias voltage.

Sample number	Bias voltage -V	Residual stress σ, GPa	Surface Roughness R_a, nm	Electrical resistivity p, 10^{-7} Ωm	Hardness H, GPa	COF -	Wear Volume μm^2 mm
S1	0	−0.342	3.7	3.95	20.1	0.56	2545
S2	30	−0.166	4.3	4.02	20.8	0.57	2439
S3	60	−0.059	8.7	11.36	25.5	0.49	2126
S4	90	0.165	8.2	7.05	21.5	0.59	1201
S5	120	0.227	6.1	2.18	20.9	0.69	1729
S6	150	0.211	4.3	2.56	20.7	0.56	1956

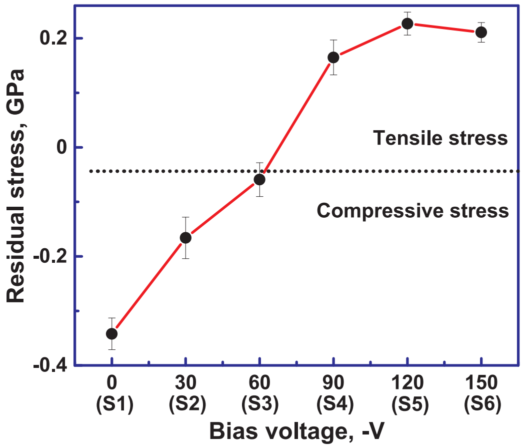

Fig. 4. Residual stress sign transition with the bias voltage applied to the substrate.

to an inaccuracy in the determination of the peak position and the calculation of stress, thus making the stress results less reliable. Actually, a moderate 2*Theta* angle range, usually 60°–90°, is more suitable for the coating stress measurement using the method of $\cos^2\alpha\sin^2\psi$ using GIXRD. Besides, diffractions with too large 2*Theta* angle will cause the value of $\cos^2\alpha$ to be too small, which affects the accuracy of linear regression in subsequent data processing. Consequently, TiN (220) are good in both peak shape and intensity while its 2*Theta* angle is about 61.8°, making it the most suitable diffraction peak to be chosen in this study. Moreover, eight inclination angles were used, ranging from 0° to 45° (0°, 15°, 20°, 25°, 30°, 35°, 40° and 45°). Details concerning residual stress measurements using X-ray diffraction can be seen in our previous publication [21]. It is worth pointing out that residual stress of the coatings is designed and controlled in a relatively narrow range using negative bias voltage according to the film thickness effect on residual stress in our previous research [21]. The results are listed in Table 2 and shown in Fig. 4. It can be seen that the residual stress of the coatings deposited at 0 V, − 30 V and − 60 V are compressive. The reason for this can be attributed to structure and defects [27]. When the bias voltage is in a relatively low range, the decrease in the absolute value of the residual stress is caused by the surface roughness. The surface roughness of the coatings increased with less negative bias voltage than − 60 V, as shown in Fig. 7. This is beneficial to the generation of tensile stress, since rough surfaces are more likely to induce in-plane contact between neighboring grain surfaces, which relieves compressive stress to some extent [21].

When the bias voltage increased, a stress sign transition from compressive to tensile can be seen. As for the coatings with the negative bias voltage higher than − 60 V, the residual stress turns to tensile and increases with more negative bias voltage. This is related to thermal stress. As the bias voltage increases, the incident ions with higher energy hit the substrate surface, thus making the substrate temperature T_s higher. Consequently, the ratio of T_s/T_m (T_m is the melting point of the coating material) becomes higher. This leads to an increase in the degree of mismatch between the coating and the substrate [28,29]. The combination of these factors makes tensile residual stress greater.

3.3. Hardness and Young's modulus

The nanohardness and the Young's modulus of the coatings were evaluated by nanoindentation. The Young's modulus measurement results were 314.18 GPa, 300.56 GPa, 311.81 GPa, 301.75 GPa, 308.63 GPa and 314.73 GPa, respectively. As a consequence, the average value of the TiN coatings' Young's modulus was 308.61 GPa, which was used in this study.

The hardness results are shown in Table 2, and Fig. 5 illustrates the hardness evolution with bias voltage. The maximum hardness attained was 25.5 GPa at a bias voltage of − 60 V, decreasing to 20.7 GPa at − 150 V. The coating hardness is affected by some competing factors, such as microstructure, surface roughness, grain size, residual stress and so on. Higher coating hardness can result if the coating has small grain size, dense microstructure, or compressive residual stress [30–32]. In Fig. 5, when the negative bias voltage is lower than − 30 V, the hardness was relatively low because of the loose microstructure. At a bias voltage of − 60 V, the hardness reached its maximum value of 25.5 GPa. This could be mainly attributed to the finer grain size, which enhanced the possibility of the dislocation blocking and thus strengthening the coatings, namely the Hall-Petch relationship [27]. When the negative bias voltage increased above − 90 V, the decrease in coating hardness was mainly caused by the compressive-to-tensile stress transition, as previously shown in Fig. 4.

3.4. Surface roughness and electrical resistivity

To further study the coating morphology, AFM was employed and the coatings' surface topography was acquired in the scanned area of 3 × 3 μm^2. The results are listed in Table 2. Fig. 6 clearly shows that for the 0 V and − 30 V coatings, the surfaces were relatively smooth and had small grain size. As the negative bias voltage increased to − 60 V, many hill-like shapes were observed, with irregular patterns on the

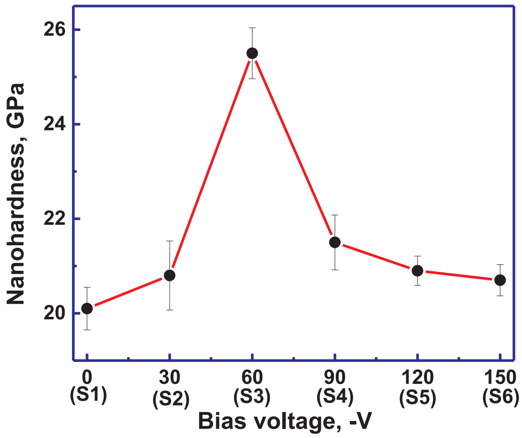

Fig. 5. The hardness evolution with bias voltage.

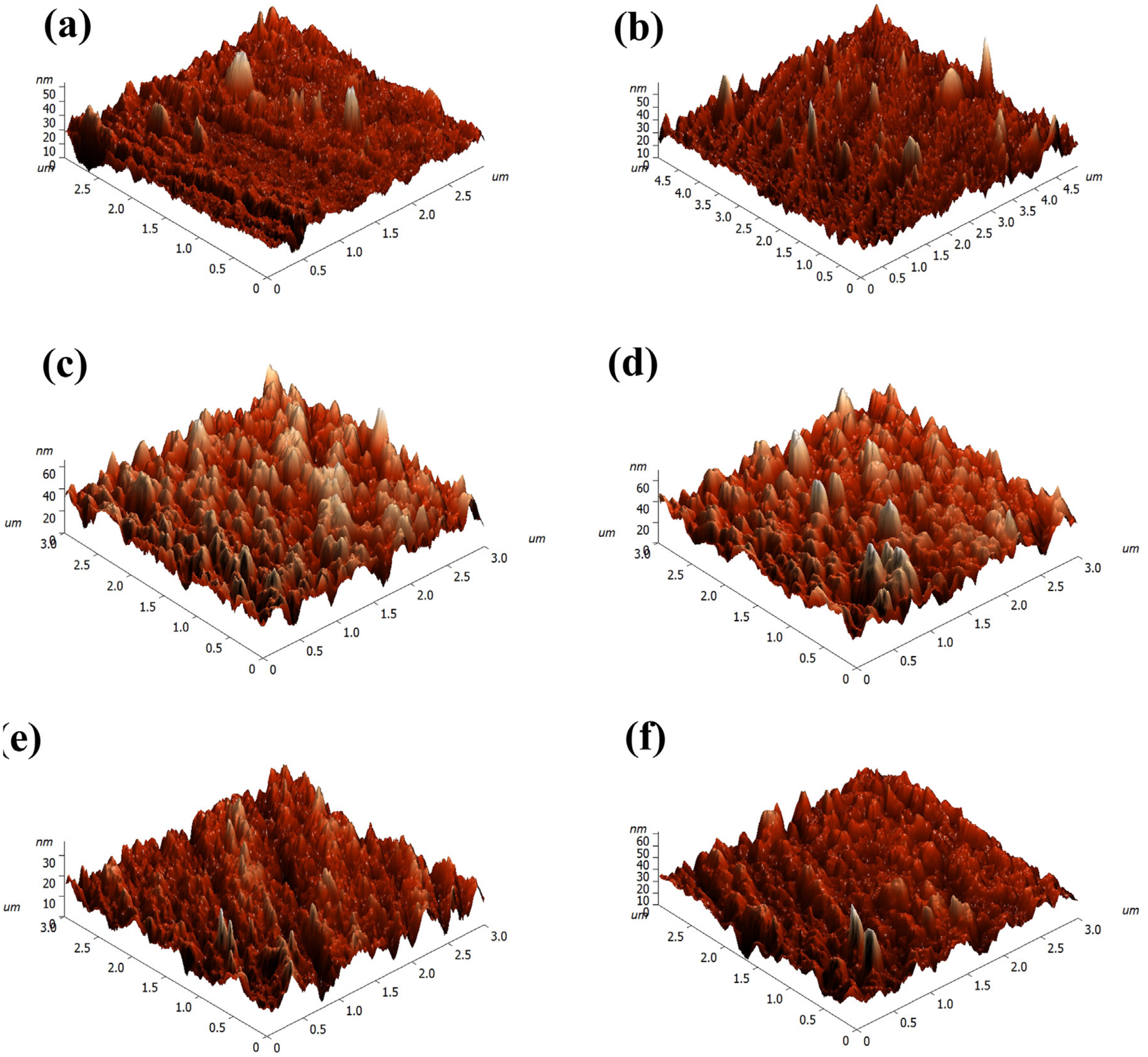

Fig. 6. AFM surface topography of TiN coatings deposited at different bias: (a) 0 V; (b) − 30 V; (c) − 60 V; (d) − 90 V; (e) − 120 V and (f) − 150 V.

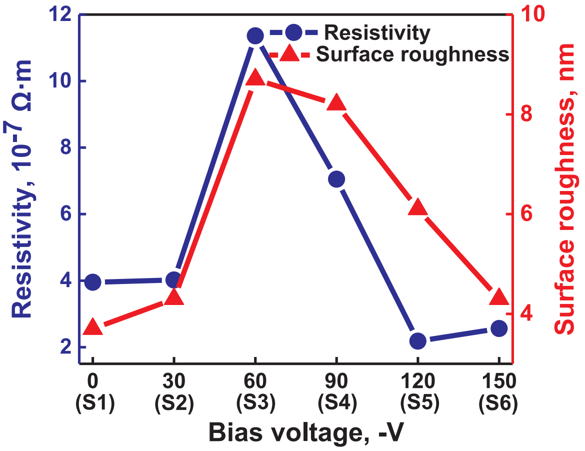

Fig. 7. Electrical resistivity and surface roughness dependence on the substrate bias.

coating surface. Moreover, a sudden increase in surface roughness was observed, reaching its maximum at − 60 V. The reason lies in the enhanced diffusion and accumulation effect with the increased negative bias [27]. As the negative bias voltage continues to increase, smoother surfaces and smaller grain sizes appear again due to bias-enhanced ion bombardment and high ionization [33]. When the negative bias voltage increases above − 120 V, the excessive energy is dissipated as heat on the coating's growing surface due to the ion bombardment. This will melt and flatten the coating surface [33], which results in a decrease in surface roughness, as seen in Fig. 7.

The electrical properties can be affected by residual stress, as is proven by Izumi and Huang [34,35]. The four-point probe is routine for electrical resistivity measurement [36,37], and was used in this study. The results are listed in Table 2 and shown in Fig. 7. According to the Matthiessen's rule [36], the electrical resistivity of the coating can be written as:

$$p = p_a + p_i + p_g + p_s \tag{2}$$

Here, p_a is the resistivity of the bulk material determined by chemical composition and phase, while p_i, p_g, and p_s is the resistivity caused by the impurities, grain boundaries and surface roughness, respectively. In this study, all coatings were prepared with the variation in negative bias, while other parameters were kept constant. Consequently, the composition, phase and impurities of the coatings should be the same. As for the grain boundaries, TiN coatings (S1-S6) should not be too different from one another because each coating had the same thickness. Thus, the major contributing factor for electrical resistivity should be surface roughness. As seen in Fig. 7, the electrical resistivity of the coatings increased from S1 to S3 and then decreased from S3 to S6. This is consistent with the surface roughness evolution.

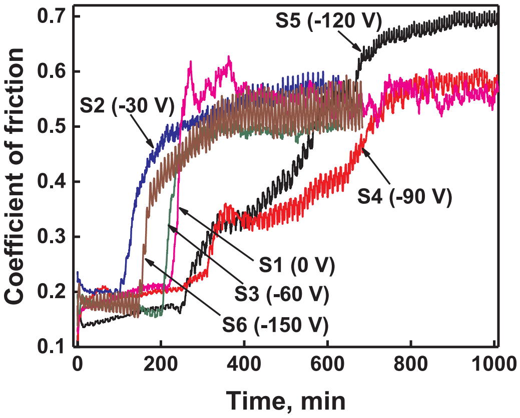

Fig. 8. The coefficient of friction of the TiN coatings.

3.5. Friction behavior and wear characteristics

Fig. 8 illustrates the coefficient of friction (COF) evolution during tribological tests for all TiN coatings. The steady-state COF values of all coatings are listed in Table 2. According to the COF evolution, the coating failure process can be divided into three stages:

(1) Accumulating stage. In this stage, the friction is not severe because of the relatively low COF of the coatings. The coatings remain intact during this stage.
(2) Damaging stage. The friction increased severely. Coating failure mainly occurred in this stage. The rising time of the COF before it reaches a steady value represents the transition from intact to fracture. The duration of the fracture process reflects the wear resistance of the coatings.
(3) Steady-state stage. This stage is determined by the failure mechanism, which can be explained by the experimental evidence of the wear track morphology.

As seen in Fig. 8, coating S1 (0 V), S2 (−30 V), S4 (−90 V) and S6 (−150 V) reached a maximum COF value of 0.55–0.6. Coating S4 (−90 V) and S5 (−120 V) showed the longest and second longest transition time, indicating good performance in friction. As a whole, coating S4 (−90 V) behaved the best due to its average COF and long transition time.

Typical appearances of wear tracks after the steady-state friction are shown in Fig. 9. Obviously, the morphology of the coating samples shows variations. Sorted by increasing severity of the wear damage, according to Fig. 9, the order is S4 < S5 < S6 < (c) S3 < S2 < S1. In Fig. 9(d) and (e), only slight worn furrows and a small amount of debris can be found in coatings S4 and S5. As the wear damage severity increases, worn furrows become deeper and the amount of debris increases significantly in coatings S3 and S6, as seen in Fig. 9(c) and (f). Moreover, the coating spalling can be found close to the edge of the wear track. In Fig. 9(a) and (b), the wear damage was most severe. Worn furrows are quite deep and there is much debris with irregular shapes and nonhomogeneous size. Meanwhile, cracks, spalling and even fracture of coatings S1 and S2 can be seen along the wear tracks. The coating has been worn out in certain places on the surface and the substrate material was exposed, showing the severity of the wear.

To characterize the wear behavior of TiN coatings quantitatively, a 3D microscope was used to obtain the wear volume of the wear tracks. The middle zone of every wear track with the same length was selected to calculate wear. The results are listed in Table 2 and Fig. 10. Coating S1 exhibited poor wear resistance, while S4 exhibited the best resistance. Although coatings S5 and S6 had smoother surfaces compared with S4, they showed larger wear volume than S4, since tensile stress is not conducive to optimizing friction and wear properties. It is

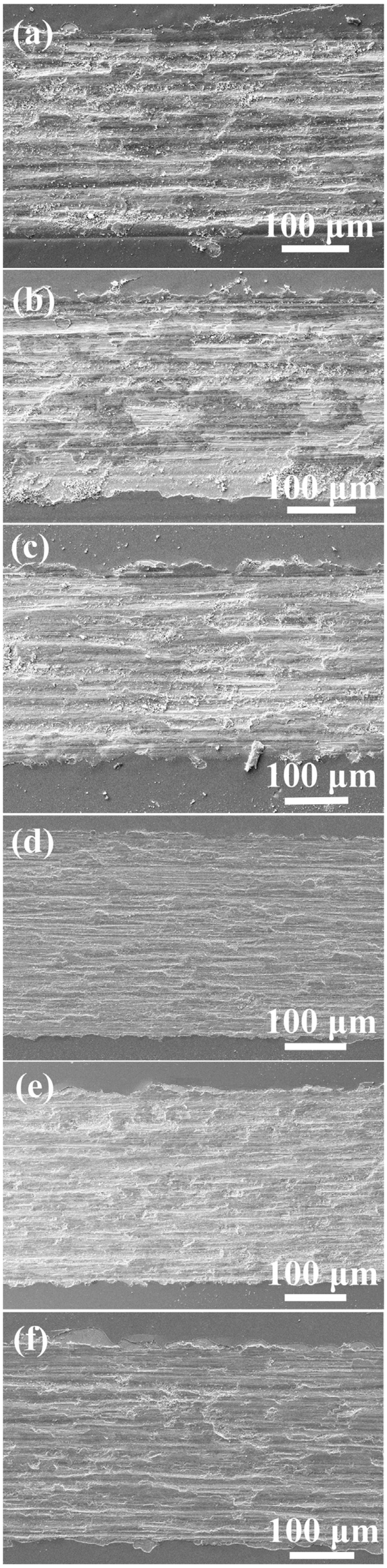

Fig. 9. Wear track morphology of the TiN coatings: (a) S1 (0 V); (b) S2 (−30 V); (c) S3 (−60 V); (d) S4 (−90 V); (e) S5 (−120 V) and (f) S6 (−150 V).

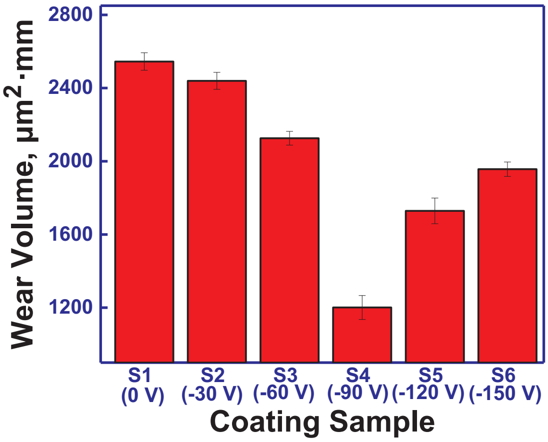

Fig. 10. Wear volume of TiN coatings.

interesting to note that the best wear resistant coating, S4, had a relatively high surface roughness and large grain size, as seen in Figs. 6 and 7. Commonly, these features do not lead to good wear resistance. This resistance is conferred to S4 by the formation of the plastic deformation of the debris inside the track, also known as a tribofilm [37]. Tribofilms will hinder further abrasion of the coating. Consequently, they can lower the wear rate and prevent coating failures by inhibiting crack nucleation and propagation [27,38].

4. Conclusions

In this work, microstructure and residual stress of TiN brittle ceramic coatings were investigated. Residual stress of the coatings is designed and successfully controlled in a relatively narrow range using negative bias voltage according to the film thickness effect on residual stress. The effects of microstructure and residual stress on mechanical, tribological and electrical properties of the coatings were revealed and the correlated mechanisms were analyzed. The main conclusion are as follows:

1. The preferred orientation of the TiN coating changes from (111) to (200) with the bias voltage and residual stress in a linear way. The process is controlled by the system energy minimization mechanism.
2. Residual stress of the coatings shows a stress sign transition from compressive to tensile with negative bias voltage. The critical bias is about − 60 V and it is related to coating structure, flaws and thermal stress at different stages.
3. The hardness of the coatings exhibits a maximum value of 25.5 GPa in coating S3. Grain size, dense microstructure and the residual stress sign are responsible for the phenomenon.
4. Surface roughness of the coatings increases first and then decreases with the negative substrate bias. The reason lies in how excessive energy is diffused. The electrical resistivity evolution shows a similar tendency with surface roughness, which is the decisive factor.
5. From the friction and wear tests, coupled with the wear volume results from the 3D microscopy, the S4 coating shows the best performance among all coatings. The tribofilm, which is the formation of plastic deformation of the debris inside the track, prevents coating failures by inhibiting crack nucleation and propagation.

In summary, it is reasonable to use the combined view of microstructure and residual stress to study the influence of inherent properties on service behavior of brittle ceramic TiN coatings. Moreover, an intermediate residual stress and proper microstructure design are of vital importance to achieve better performance during service. These findings are instructive for the design, preparation and practical use of brittle ceramic coating materials in the future.

Acknowledgements

This work is supported by the Beijing Nova Program (Z171100001117075), the National Natural Science Foundation of China (51771025), and the Fundamental Research Funds for the Central Universities (FRF-TP-17-002C1). The authors also want to thank Haijiao Xie from Shiyanjia lab for the support of the materials characterization.

References

[1] D.J. Kim, Y.B. Jung, M.B. Lee, Y.H. Lee, J.H. Lee, J.H. Lee, Applicability of ALE TiN films as Cu/Si diffusion barriers, Thin Solid Films 372 (2000) 276–283.
[2] S.M. Borah, A.R. Pal, H. Bailung, J. Chutia, Optimization of plasma parameters for high rate deposition of titanium nitride films as protective coating on bell-metal by reactive sputtering in cylindrical magnetron device, Appl. Surf. Sci. 254 (2008) 5760–5765.
[3] M. Bartosik, M. Arndt, R. Rachbauer, C. Krywka, C.M. Koller, J. Keckes, P.H. Mayrhofer, Cross-sectional X-ray nano-diffraction and -reflectivity analysis of multilayered AlTiN–TiSiN thin films: correlation between residual strain and bilayer period, Scr. Mater. 107 (2015) 153–156.
[4] Y. Chang, W. Chiu, J. Hung, Mechanical properties and high temperature oxidation of CrAlSiN / TiVN hard coatings synthesized by cathodic arc evaporation, Surf. Coat. Technol. 303 (2016) 18–24.
[5] G.S. Fox Rabinovich, J.L. Endrino, B.D. Beake, M.H. Aguirre, S.C. Veldhuis, Effect of temperature of annealing below 900°C on structure, properties and tool life of an AlTiN coating under various cutting conditions, Surf. Coat. Technol. 202 (2008) 2985–2992.
[6] X. Sun, K. Gao, X. Pang, H. Yang, Interface and strain energy revolution texture map to predict structure and optical properties of sputtered PbSe thin films, ACS Appl. Mater. Interfaces 8 (2016) 625–633.
[7] J.H. Choi, Y. Mao, J.P. Chang, Development of hafnium based high-k materials – a review, Mater. Sci. Eng. R. Rep. 72 (2011) 97–136.
[8] H. Liang, J. Xu, D. Zhou, X. Sun, S. Chu, Y. Bai, Thickness dependent microstructural and electrical properties of TiN thin films prepared by DC reactive magnetron sputtering, Ceram. Int. 42 (2016) 2642–2647.
[9] A.A. Vereschaka, S.N. Grigoriev, Study of cracking mechanisms in multi-layered composite nano-structured coatings, Wear 378–379 (2017) 43–57.
[10] L. Su, C. Yi, Effects of CMAS penetration on the delamination cracks in EB-PVD thermal barrier coatings with curved interface, Ceram. Int. 43 (2017) 8893–8897.
[11] A. Yin, J. Yan, L. Chen, S. Zhu, Z. Long, L. Fang, T. Liu, Experimental and numerical investigation of buckling and delamination of Ti/TiN coatings on depleted uranium under compression, Appl. Surf. Sci. 422 (2017) 997–1006.
[12] S. Koseki, K. Inoue, H. Usuki, Frank wear of PVD-coated cutting tools during continuous turning of alloy 718, Seimitsu Kogaku Kaishi/J. Jpn. Soc. Precis. Eng. 82 (2016) 460–466.
[13] X. Song, F. Meng, M. Kong, Z. Liu, L. Huang, X. Zheng, Y. Zeng, Relationship between cracks and microstructures in APS YSZ coatings at elevated temperatures, Mater. Charact. 131 (2017) 277–284.
[14] S. Li, C. Li, P. Deng, Y. Zhang, Q. Zhang, S. Sun, H. Yan, P. Ma, Y. Wang, Microstructure and properties of laser-cladded bimodal composite coatings derived by composition design, J. Alloy. Compd. 745 (2018) 483–489.
[15] B. Vierneusel, L. Benker, S. Tremmel, M. Göken, B. Merle, Isolating the effect of residual stresses on coating wear by a mechanical stress relaxation technique, Thin Solid Films 638 (2017) 159–166.
[16] M. Tkadletz, N. Schalk, R. Daniel, J. Keckes, C. Czettl, C. Mitterer, Advanced characterization methods for wear resistant hard coatings: a review on recent progress, Surf. Coat. Technol. 285 (2016) 31–46.
[17] Y.C. Huang, S.Y. Chang, C.H. Chang, Effect of residual stresses on mechanical properties and interface adhesion strength of SiN thin films, Thin Solid Films 517 (2009) 4857–4861.
[18] G. Skordaris, K.D. Bouzakis, T. Kotsanis, P. Charalampous, E. Bouzakis, B. Breidenstein, B. Bergmann, B. Denkenac, Effect of PVD film's residual stresses on their mechanical properties, brittleness, adhesion and cutting performance of coated tools, CIRP J. Manuf. Sci. Technol. 18 (2017) 145–151.
[19] X. Zhang, M. Watanabe, S. Kuroda, Effects of residual stress on the mechanical properties of plasma-sprayed thermal barrier coatings, Eng. Fract. Mech. 110 (2013) 314–327.
[20] C.H. Ma, J.H. Huang, H. Chen, Residual stress measurement in textured thin film by grazing-incidence X-ray diffraction, Thin Solid Films 418 (2002) 73–78.
[21] Y. Xi, K. Gao, X. Pang, H. Yang, X. Xiong, H. Li, A.A. Volinsky, Film thickness effect on texture and residual stress sign transition in sputtered TiN thin films, Ceram. Int. 43 (2017) 11992–11997.
[22] R. Saha, W.D. Nix, Effects of the substrate on the determination of thin film mechanical properties by nanoindentation, Acta Mater. 50 (2002) 23–38.
[23] Y. Wang, W. Tang, L. Zhang, Crystalline size effects on texture coefficient,electrical and optical properties of sputter-deposited Ga-doped ZnO thin films, J. Mater. Sci. Technol. 31 (2015) 175.
[24] Y.H. Cheng, B.K. Tay, Development of texture in TiN films deposited by filtered cathodic vacuum arc, J. Cryst. Growth 252 (2003) 257–264.
[25] G. Abadias, Stress and preferred orientation in nitride-based PVD coatings, Surf. Coat. Technol. 202 (2008) 2223–2235.

[26] Y. Xi, Y. Bai, K. Gao, X. Pang, H. Yang, L. Yan, A.A. Volinsky, In-situ stress gradient evolution and texture-dependent fracture of brittle ceramic thin films under external load, Ceram. Int. 44 (2018) 8176–8183.

[27] Y. Lv, Li. Ji, X. Liu, H. Li, H. Zhou, Influence of substrate bias voltage on structure and properties of the CrAlN films deposited by unbalanced magnetron sputtering, Appl. Phys. Lett. 258 (2012) 3864–3870.

[28] S. Khamseh, M. Nose, T. Kawabata, T. Nagae, K. Matsuda, S. Ikeno, A comparative study of CrAlN films synthesized by dc and pulsed dc reactive magnetron facing target sputtering system with different pulse frequencies, J. Alloy. Compd. 508 (2010) 191–195.

[29] C. Mitterer, P.H. Mayrhofer, J. Musil, Thermal stability of PVD hard coatings, Vacuum 71 (2003) 279–284.

[30] J.A. Freeman, P.J. Kelly, G.T. West, J.W. Bradley, I. Iordanova, The effects of composition and pulsed biasing on chromium nitride films, Surf. Coat. Technol. 204 (2009) 907–910.

[31] J.W. Lee, Y.C. Kuo, C.J. Wang, L.C. Chang, K.T. Liu, Effects of substrate bias frequencies on the characteristics of chromium nitride coatings deposited by pulsed DC reactive magnetron sputtering, Surf. Coat. Technol. 203 (2008) 721–725.

[32] H.W. Chang, P.K. Huang, J.W. Yeh, A. Davison, C.H. Tsau, C.C. Yang, Influence of substrate bias, deposition temperature and post-deposition annealing on the structure and properties of multi-principal-component (AlCrMoSiTi)N coatings, Surf. Coat. Technol. 202 (2008) 3360–3366.

[33] M. Zhang, M.K. Li, K.H. Kim, F. Pan, Structural and mechanical properties of compositionally gradient CrN_x coatings prepared by arc ion plating, Appl. Surf. Sci. 255 (2009) 9200–9205.

[34] H. Izumi, F.O. Adurodija, T. Kaneyoshi, T. Ishihara, H. Yoshioka, M. Motoyama, Electrical and structural properties of indium tin oxide films prepared by pulsed laser deposition, J. Appl. Phys. 91 (2002) 1213–1218.

[35] J.H. Huang, K.W. Lau, G.P. Yu, Effect of nitrogen flow rate on structure and properties of nanocrystalline TiN thin films produced by unbalanced magnetron sputtering, Surf. Coat. Technol. 191 (2005) 17–24.

[36] V. Timoshevskii, Y. Ke, H. Guo, D. Gall, The influence of surface roughness on electrical conductance of thin Cu films: an ab initio study, J. Appl. Phys. 103 (2008) 9–12.

[37] A. Garzon-Fontecha, H.A. Castillo, E. Restrepo-Parra, W. De La Cruz, The role of the nitrogen flow rate on the transport properties of CrN thin films produced by DC magnetron sputtering, Surf. Coat. Technol. 334 (2018) 98–104.

[38] G.A. Zhang, P.X. Yan, P. Wang, Y.M. Chen, J.Y. Zhang, The structure and tribological behaviors of CrN and Cr-Ti-N coatings, Appl. Surf. Sci. 253 (2007) 7353–7359.